

Strongly Coupled Pyridine- $V_2O_5 \cdot nH_2O$ Nanowires with Intercalation Pseudocapacitance and Stabilized Layer for High Energy Sodium Ion Capacitors

Jun Dong, Yalong Jiang, Qiulong Wei,* Shuangshuang Tan, Yanan Xu, Guobin Zhang, Xiaobin Liao, Wei Yang, Qidong Li, Qinyou An, and Liqiang Mai*

Developing pseudocapacitive cathodes for sodium ion capacitors (SICs) is very significant for enhancing energy density of SICs. Vanadium oxides cathodes with pseudocapacitive behavior are able to offer high capacity. However, the capacity fading caused by the irreversible collapse of layer structure remains a major issue. Herein, based on the Acid–Base Proton theory, a strongly coupled layered pyridine- $V_2O_5 \cdot nH_2O$ nanowires cathode is reported for highly efficient sodium ion storage. By density functional theory calculations, in situ X-ray diffraction, and ex situ Fourier-transform infrared spectroscopy, a strong interaction between protonated pyridine and $V=O$ group is confirmed and stable during cycling. The pyridine- $V_2O_5 \cdot nH_2O$ nanowires deliver long-term cyclability (over 3000 cycles), large pseudocapacitive behavior (78% capacitive contribution at 1 mV s^{-1}) and outstanding rate capability. The assembled pyridine- $V_2O_5 \cdot nH_2O$ /graphitic mesocarbon microbead SIC delivers high energy density of $\approx 96 \text{ Wh kg}^{-1}$ (at 59 W kg^{-1}) and power density of 14 kW kg^{-1} (at 37.5 Wh kg^{-1}). The present work highlights the strategy of realizing strong interaction in the interlayer of $V_2O_5 \cdot nH_2O$ to enhance the electrochemical performance of vanadium oxides cathodes. The strategy could be extended for improving the electrochemical performance of other layered materials.

(e.g., activated carbon (AC)) and an intercalation-type battery anode (e.g., $Li_4Ti_5O_{12}$, TiO_2).^[1] Developing sodium ion capacitors (SICs) is very promising owing to the very abundant sodium element ($\approx 23\,000$ ppm in earth crust) superior to lithium element (≈ 17 ppm) and decent chemical properties of sodium similar to lithium.^[6–8] The enhanced energy density ($>40 \text{ Wh kg}^{-1}$) of SICs is higher than that of commercial EDLCs ($5\text{--}10 \text{ Wh kg}^{-1}$).^[1] However, the energy of the hybrid capacitors is still unsatisfactory at present, because of the use of low-capacity EDLC-type cathodes ($\approx 30\text{--}60 \text{ mAh g}^{-1}$).^[4] A promising strategy is to develop pseudocapacitive cathode materials for storing sodium ion, because pseudocapacitance usually offers a high capacity at fast charge–discharge rate (a faradaic process involving redox reaction at or near active materials' surface).^[9,10] Importantly, Dunn and co-workers^[10,11] have proved an intercalation pseudocapacitance without phase transformation and diffusion limitation, which brings a new opportunity to enlarge the capacity and energy of hybrid capacitors. However, the pseudocapacitive cathode materials for sodium ion storage remain largely undeveloped.

Electrochemical capacitors (ECs) can ensure fast energy delivery and collection, which are popularized in mobile electronics, hybrid electric vehicles, and smart grids.^[1,2] Conventionally, the ECs utilize both electrostatic double-layer capacitance (EDLC) electrodes, which deliver very low energy densities due to the only reversible physical ion adsorption at the material surface to store charge. Thus, the concept of lithium and sodium ion capacitors was pointed out.^[3–5] The hybrid ion capacitors are composed of an EDLC-type cathode

Layered vanadium oxides with pseudocapacitive behaviors are the very promising cathode materials for sodium ion storage due to its high theoretical capacity.^[12,13] The high charge storage capability is attributed to the multielectron faradaic redox process from the change of vanadium valance.^[14] Interestingly, layered $V_2O_5 \cdot nH_2O$ with large interlayer spacing ($\approx 13.36 \text{ \AA}$) provides a rapid Na^+ ion diffusion channel without phase change processes, and delivers a high sodium storage capacity of $\approx 200 \text{ mAh g}^{-1}$.^[15] Unfortunately, a large capacity loss of almost 40% after only 30 cycles was observed,^[15] which definitely hindered the application for layered $V_2O_5 \cdot nH_2O$ as cathode for high energy and power SICs. Several investigations indicate that the origins of capacity loss for vanadium oxides are the collapse of layer structure, self-trapping of polarons, and decrease of conductivity during Na^+ (de)intercalations.^[15–19] Hence, metal ions preintercalation as “pillar effect” was proposed to enhance the layered structure and restrain the

J. Dong, Y. L. Jiang, Dr. Q. L. Wei, S. S. Tan, Y. N. Xu, G. B. Zhang, X. B. Liao, W. Yang, Q. D. Li, Prof. Q. Y. An, Prof. L. Q. Mai
State Key Laboratory of Advanced Technology for Materials Synthesis and Processing
International School of Materials Science and Engineering
Wuhan University of Technology
Hubei, Wuhan 430070, P. R. China
E-mail: wql236@whut.edu.cn; mlq518@whut.edu.cn

 The ORCID identification number(s) for the author(s) of this article can be found under <https://doi.org/10.1002/sml.201900379>.

DOI: 10.1002/sml.201900379

“lattice breathing”, which has shown an enhancement of the cycling stability.^[20,21] However, their long-term cyclability remains unsatisfactory, probably because interactions between preintercalated ions and the layers could be weak and not stable for the long term during Na⁺ (de)intercalations. Therefore, realizing the strong interaction between the layers is able to optimize the cycling performance.

Based on Acid–Base Proton theory, the layered V₂O₅·*n*H₂O provides free protons between its layers, which is regarded as Brønsted acid (as proton donor).^[22] An appropriate neutral molecule as Lowry base (proton acceptor) could be protonated by the hydrated interlayers.^[23] Herein, the pyridine is the appropriate choice, whose nitrogen provides the basic lone pair. The pyridine is protonated and preintercalated into the layered V₂O₅·*n*H₂O with a formation of strong hydrogen-bond (H-bond) interaction. Confirmed by in situ X-ray diffraction (XRD) results, the strong interaction between the intercalated protonated pyridine (PyH⁺) and V₂O₅·*n*H₂O stabilizes the whole layered structure, thereby inhibiting the “lattice breathing” during sodium ion intercalation/extraction and enhancing the cycling performance. Besides, the pyridine intercalation simultaneously optimizes the thermostability and electronic conductivity, therefore leading to improved pseudocapacitance and rate capability. Through kinetics analysis, ex situ Fourier transform infrared (FTIR) characterizations, in situ XRD, and electronic structure calculations, the effects of intercalated pyridine are systematically expounded. Furthermore, an asymmetric SIC, made up of pseudocapacitive pyridine-V₂O₅·*n*H₂O nanowires cathode and [Na-diglyme]⁺ co-intercalated graphitic mesocarbon microbead (MCMB) anode, shows high power and energy densities, indicating the prospect of pseudocapacitive cathode for advanced SICs.

The pyridine-V₂O₅·*n*H₂O nanowires were synthesized by mixing pyridine and V₂O₅ sol through a one-pot hydrothermal reaction. The powder XRD pattern and Rietveld refinement implemented by TOPAS 4.2 are employed to investigate the crystal structure of as-synthesized material (Figure 1a).^[24] The strong diffraction peak at 2θ = 7.78° shows an interlayer spacing of ≈11.36 Å. The detailed lattice parameters are *a* = 11.85(3) Å, *b* = 3.56(1) Å, *c* = 11.36(3) Å, α = 88.32(8)°, β = 88.48(4)°, γ = 87.94(5)°. The V₂O₅·*n*H₂O without pyridine shows a diffraction peak at 2θ = 6.60° (Figure S1a, Supporting Information), indicating a *d*-spacing of 13.36 Å. The results indicate a contraction in the interlayer between [V₂O₅] layers after pyridine intercalation. The slight interlayer contraction could be due to the strong attractive effect between PyH⁺ and the V=O from the layers, which is conducive to stabilizing the layer structure. Transmission electron microscopy (TEM) images (Figure 1b and Figure S2, Supporting Information) show the pyridine-V₂O₅·*n*H₂O nanowires with a length of several micrometers and a width of ≈100 nm. The high-resolution TEM (HRTEM) image of pyridine-V₂O₅·*n*H₂O (Figure 1c) exhibits the well-defined layered structures with a *d*-spacing of ≈11.4 Å, very close to the value calculated from the XRD result.

To determine the intercalation content of the pyridine into the layered V₂O₅·*n*H₂O, a gradient amount of pyridine was added for the hydrothermal synthesis, while the XRD patterns and C/N contents are shown in Figure S1b and Table S1 in the Supporting Information. The C and N signals are from

the intercalated pyridine. The mole ratio of C/N is ≈5.0, which is close to the theoretical value of the pyridine molecule, indicating the intercalation of pyridine. The (001) diffraction peak shifts to high angle as the amount of intercalated pyridine increases. However, the diffraction peak remains unchanged until 3 mL of pyridine is involved in the hydrothermal reaction. In addition, the C/N contents are almost the same between the samples with 1 and 3 mL pyridine (Table S1, Supporting Information), indicating that the amount of pyridine intercalation into the interlayer is limited. Thus, the pyridine-V₂O₅·*n*H₂O with the addition of 1 mL pyridine is chosen as the optimal object for this study. The thermogravimetry (TG) of pristine V₂O₅·*n*H₂O and pyridine-V₂O₅·*n*H₂O (Figure S3, Supporting Information) was carried out up to 700 °C in argon. The weight loss of crystal water and pyridine molecule occurs at 120 and 220 °C, respectively.^[25] A higher weight loss of pyridine-V₂O₅·*n*H₂O is attributed to the existence of pyridine. Compared to the V₂O₅·*n*H₂O sample, the weight loss of pyridine-V₂O₅·*n*H₂O occurs at a higher temperature, indicating an enhanced thermostability with pyridine intercalation. Based on the CHN analysis and weight loss in TG (Table S1, Supporting Information), the chemical formula of pyridine-V₂O₅·*n*H₂O and V₂O₅·*n*H₂O are formulated as V₂O₅·0.77H₂O·0.54Pyridine and V₂O₅·0.79H₂O (the detailed calculation is shown in the Supporting Information), respectively.

FTIR spectra were further recorded to investigate the structure characteristic and the chemical composition of pyridine-V₂O₅·*n*H₂O (Figure 1d). Table S2 in the Supporting Information shows frequencies and assignment of the FTIR absorption bands of pyridine-V₂O₅·*n*H₂O and V₂O₅·*n*H₂O, respectively. The distinct peaks at 1633, 1537, and 1482 cm⁻¹ are attributed to ν(C–C) vibration of pyridine ring.^[26] The N–H stretching vibration (ν_{7a}) occurs in the region from 3500 to 1650 cm⁻¹.^[27] Besides, the frequency is no single band but composed of two to four components; the band frequency varies with the interaction between the N–H and an anion.^[27] Thus, the bands of pyridine-V₂O₅·*n*H₂O at 3230, 3164, 3128, and 3086 cm⁻¹ are associated with the N–H vibrations. These protons of N–H bonds are possible from V₂O₅·*n*H₂O xerogel with free protons, which can be exchanged with other ions or react with pyridine.^[22,26] Therefore, these results corroborate the existence of pyridine and the formation of PyH⁺ by the proton-transfer reaction. X-ray photoelectron spectroscopy (XPS) spectrum of N1s (Figure 1e) shows the protonated nitrogen atom (N–H bond),^[28] consistent with the FTIR results. The V=O peak (1012 cm⁻¹) of V₂O₅·*n*H₂O shows a red-shift and splits into two peaks (1002 and 966 cm⁻¹) for the pyridine-V₂O₅·*n*H₂O sample, which is likely as V⁵⁺=O (1002 cm⁻¹) and V⁴⁺=O (966 cm⁻¹). The reduction of vanadium valence after pyridine intercalation is also confirmed by the analysis of V 2p_{3/2} spectra: an enhanced relative intensity of V⁴⁺ in pyridine-V₂O₅·*n*H₂O (Figure S4 and Table S3, Supporting Information). Interestingly, the FTIR spectrum of previous ion preintercalated V₂O₅·*n*H₂O presents that the peak of V=O only shows slight red-shift but without split.^[20] Here, the separated V=O peaks of pyridine-V₂O₅·*n*H₂O are possible due to stronger interaction between PyH⁺ and the V=O from the layers.^[26,28] The valence state of V has been reported to be related with the electronic conductivity and cycling stability of vanadium oxides.^[14,29] The electronic

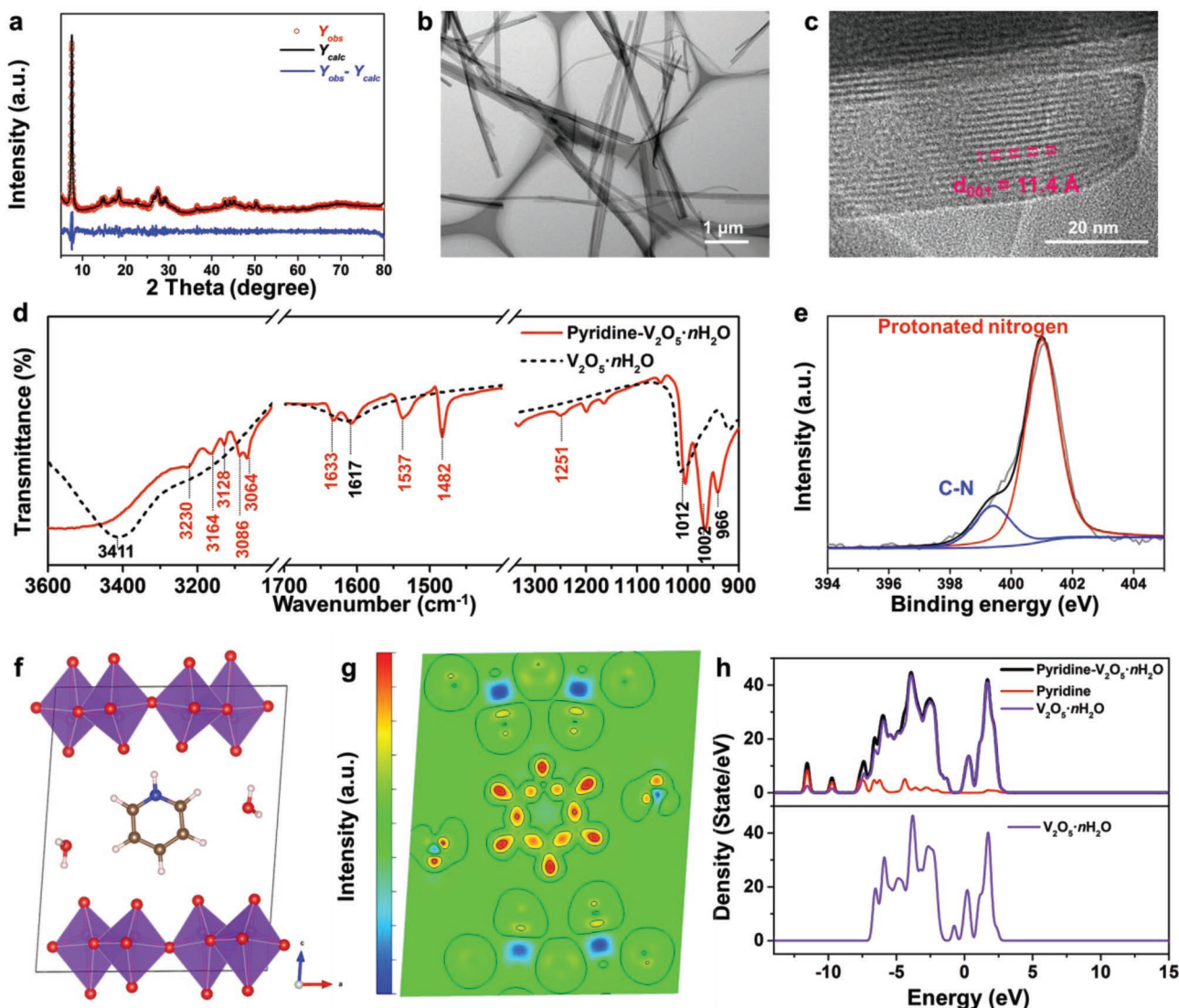


Figure 1. Synthesis and structural characterizations of pyridine- $V_2O_5 \cdot nH_2O$ nanowires. a) XRD pattern of pyridine- $V_2O_5 \cdot nH_2O$ nanowires and Rietveld refinement data, indicating a pyridine intercalated layer structure with a spacing of ≈ 11.36 Å. b) TEM and c) HRTEM images of pyridine- $V_2O_5 \cdot nH_2O$ nanowires, respectively. d) FTIR spectra of pyridine- $V_2O_5 \cdot nH_2O$ and $V_2O_5 \cdot nH_2O$. e) N 1s XPS spectrum of pyridine- $V_2O_5 \cdot nH_2O$, confirming the existence of protonated nitrogen from intercalated pyridine. Electronic structure calculation: f) optimized atomic configurations, g) 2D charge-density difference, and h) density of states of pyridine- $V_2O_5 \cdot nH_2O$.

conductivity of $V_2O_5 \cdot nH_2O$ and pyridine- $V_2O_5 \cdot nH_2O$ is tested by depositing two Au measuring electrode on a nanosheet or nanowire. I - V curves (Figure S5, Supporting Information) obviously present that the slope of pyridine- $V_2O_5 \cdot nH_2O$ is much higher than that of $V_2O_5 \cdot nH_2O$. The measured electronic conductivity of pyridine- $V_2O_5 \cdot nH_2O$ is 7.51 S cm^{-1} , which is higher than the $V_2O_5 \cdot nH_2O$ (0.047 S cm^{-1}) and other molecules incorporated $V_2O_5 \cdot nH_2O$.^[30,31]

To gain fundamental insight into the effect of pyridine intercalation on electronic conductivity and structure stability density functional theory calculations for the optimized atomic configuration of pyridine- $V_2O_5 \cdot nH_2O$ and the density of states (DOS) were conducted. Figure 1f displays the interaction of PyH^+ with $V=O$ group in pyridine- $V_2O_5 \cdot nH_2O$. The charge density difference plot manifests the interlayer electron-electron

coupling in pyridine- $V_2O_5 \cdot nH_2O$ (Figure 1g and Figure S6, Supporting Information). The obvious charge transfer induces H-bond interaction between PyH^+ and vanadium-oxygen layers, thus providing the enhanced structural stability of pyridine- $V_2O_5 \cdot nH_2O$. Further, the DOS of $V_2O_5 \cdot nH_2O$ and pyridine- $V_2O_5 \cdot nH_2O$ are applied to analyze the charge transport (Figure 1h). Compared to $V_2O_5 \cdot nH_2O$, the additional continuous states from the intercalation of pyridine are observed, which leads to a higher dispersion of band structure in pyridine- $V_2O_5 \cdot nH_2O$ and enhances the electronic conductivity, consistent with the conductive measurement results (Figure S5, Supporting Information).

The electrochemical performance of pyridine- $V_2O_5 \cdot nH_2O$ was tested by assembling coin cells (2016-type) with metallic sodium as the counter electrode. Galvanostatic tests were

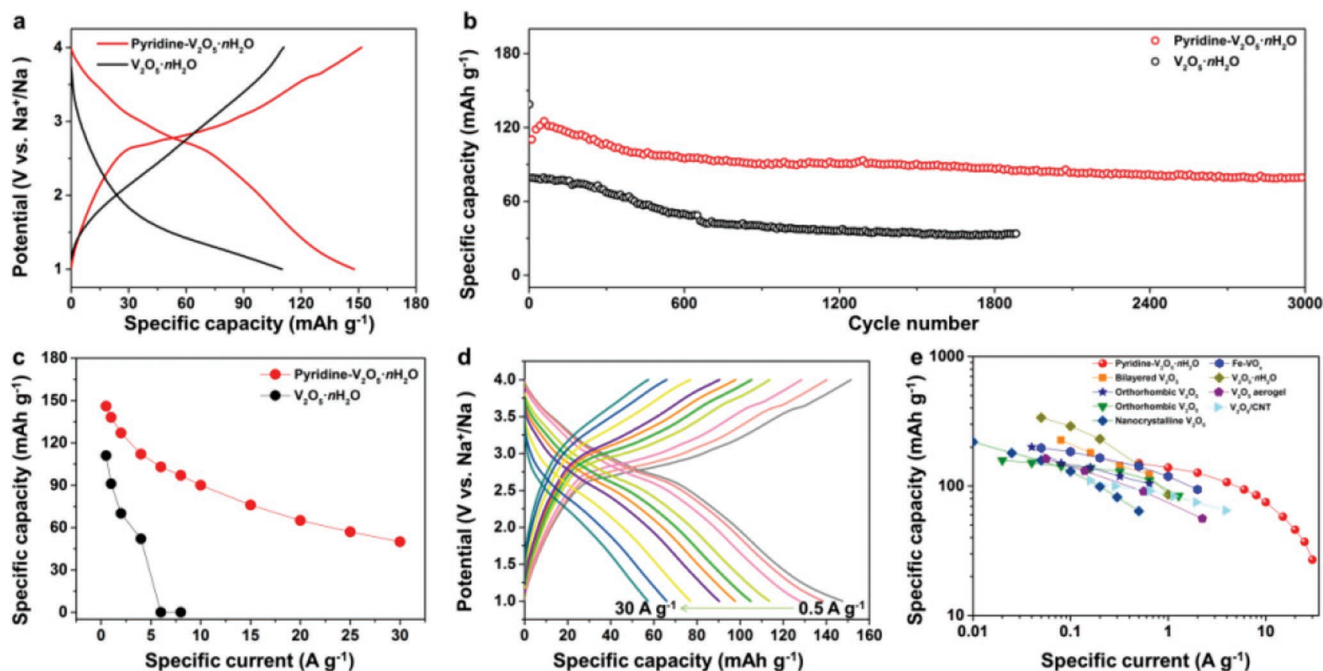


Figure 2. Sodium ion storage performance. a) Charge–discharge curves of pyridine- $V_2O_5 \cdot nH_2O$ and $V_2O_5 \cdot nH_2O$ at 0.5 A g^{-1} in the potential range of 1–4 V (vs Na^+/Na). b) Long-term cycling performance at 1 A g^{-1} and c) rate performance of pyridine- $V_2O_5 \cdot nH_2O$ and $V_2O_5 \cdot nH_2O$, respectively. d) Charge–discharge curves of pyridine- $V_2O_5 \cdot nH_2O$ at various specific currents from 0.5 to 30 A g^{-1} . e) A comparison with the state-of-the-art vanadium-based materials for sodium ion storage in literatures.^[15,20,33–38]

conducted at a specific current of 0.5 A g^{-1} in a potential range of 1–4 V (vs Na^+/Na). The charge–discharge curves of pyridine- $V_2O_5 \cdot nH_2O$ exhibit much smaller overpotential than that of $V_2O_5 \cdot nH_2O$ (Figure 2a). A reversible discharge capacity of the pyridine- $V_2O_5 \cdot nH_2O$ is 150 mAh g^{-1} , which is higher than that of $V_2O_5 \cdot nH_2O$ (110 mAh g^{-1}). The cycling performance at high specific current of 1 A g^{-1} is shown in Figure 2b. The pyridine- $V_2O_5 \cdot nH_2O$ displays a capacity retention of 74% after 1000 cycles, which is better than $V_2O_5 \cdot nH_2O$ (48%). Besides, the cycling numbers of pyridine- $V_2O_5 \cdot nH_2O$ reach up to 3000 cycles with a capacity retention of 67%, which is rarely reported for other cathodes for sodium ion storage.^[32] The rate performance, at the specific current ranging from 0.5 to 30 A g^{-1} , was further tested (Figure 2c). The specific capacity of pyridine- $V_2O_5 \cdot nH_2O$ is 138, 112, and 97 mAh g^{-1} at 1, 4, and 8 A g^{-1} , respectively. Even at extremely high current density of 30 A g^{-1} , a specific capacity of 50 mAh g^{-1} is retained. The rate capability of pyridine- $V_2O_5 \cdot nH_2O$ is superior to $V_2O_5 \cdot nH_2O$ (91, 52, and $\approx 0 \text{ mAh g}^{-1}$ at 1, 4, and 8 A g^{-1} , respectively). The corresponding charge–discharge curves (Figure 2d) show the small increment of overpotential with the rising of specific current. A comparison of the rate capability of pyridine- $V_2O_5 \cdot nH_2O$ with the state-of-the-art vanadium oxide cathodes (e.g., V_2O_5 , $V_2O_5 \cdot nH_2O$, $Fe-VO_x$, V_2O_5/CNT) for sodium ion storage is shown in Figure 2e and Table S4 in the Supporting Information.^[15,20,33–38] The rate capability and cycling performance of pyridine- $V_2O_5 \cdot nH_2O$ are one of the best vanadium oxide cathodes for sodium storage.

The electrochemical reaction mechanism was systematically investigated to understand the functions of pyridine intercalation and provide further insights into the optimized

electrochemical performance. Figure 3a shows the ex situ FTIR spectra of pyridine- $V_2O_5 \cdot nH_2O$ at different charge or discharge states. The wavenumber of V–O–V vibrations at 515 cm^{-1} has no shift during charge–discharge process, demonstrating that the layered structure remains stable upon sodiation/desodiation. The characteristic frequencies (highlighted by red color) of $\nu(C-C)$ and $\nu(N-H)$ retain. Both splitting peaks (1002 and 967 cm^{-1}), caused by hydrogen bonds between V=O group and N–H species, are still observed, demonstrating that pyridine molecules steadily exist in the interlayers and constantly interact with $[V_2O_5]$ layers during charge–discharge process. Besides, the red-shift of V=O bond (Figure S7 (ii), Supporting Information) indicates the faradaic reduction of V^{5+} after Na^+ intercalation. In situ XRD of pyridine- $V_2O_5 \cdot nH_2O$ was performed during the galvanostatic test at a specific current of 0.1 A g^{-1} (Figure 3b). The characteristic layered diffraction peaks at 7.78° do not shift in the whole charge and discharge processes, indicating a nonphase change charge storage mechanism. The charge–discharge curves of pyridine- $V_2O_5 \cdot nH_2O$ and $V_2O_5 \cdot nH_2O$ at different cycles are shown in Figure S8a,b in the Supporting Information. During the initial 1000 cycles, the charge–discharge curves of pyridine- $V_2O_5 \cdot nH_2O$ remain similar, while along with the slight capacity decrease. The curves become linear slope and the characteristic layered diffraction peak gets weaker (Figure S8c, Supporting Information) after 3000 cycles, indicating a layered disorder process during long-term sodium (de)intercalation. Compared with the rapidly interlayered collapse of $V_2O_5 \cdot nH_2O$,^[15] the intercalated pyridine stabilizes the layered structure during Na^+ (de)intercalation, leading to largely improved electrochemical cycling performance.

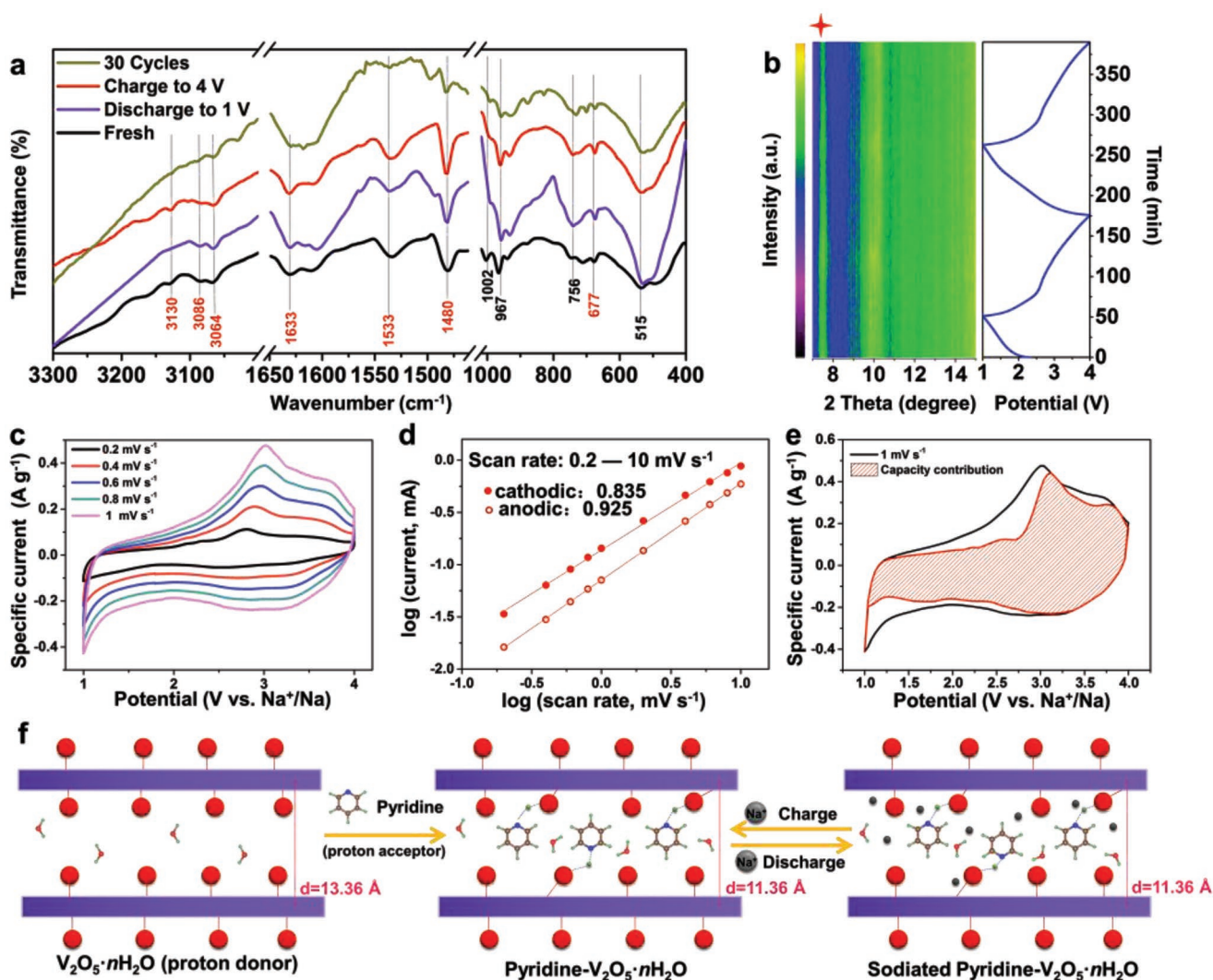


Figure 3. Sodium ion storage mechanism of pyridine- $V_2O_5 \cdot nH_2O$ and the functions of pyridine. a) Ex situ FTIR spectra of pyridine- $V_2O_5 \cdot nH_2O$ at different charged/discharged states and b) in situ XRD patterns during galvanostatic charge–discharge at 0.1 A g^{-1} in the potential range of 1–4 V (vs Na^+/Na), indicating a nonphase change charge storage process with stabilized layer structure. c–e) Kinetics analysis of the pyridine- $V_2O_5 \cdot nH_2O$: c) CV curves at various scan rates from 0.2 to 1 mV s^{-1} . d) The logarithmic peak currents versus logarithmic scan rates plots. The b_{cathodic} (0.835) and b_{anodic} (0.925) show the pseudocapacitive behavior. e) Capacitive contribution of over 78% (shaded area) to total charge storage at a 1 mV s^{-1} . f) Functions of pyridine intercalated into $V_2O_5 \cdot nH_2O$, stabilizing the interlayer structure during rapid Na^+ (de)intercalation.

The kinetics analysis was further conducted. Figure 3c and Figure S9 in the Supporting Information show the cyclic voltammetry (CV) curves of pyridine- $V_2O_5 \cdot nH_2O$ in the potential range of 1–4 V (vs Na^+/Na) at different scan rates. The CV curves exhibit the rectangular shape with a pair of broad peaks, which is a symbol of pseudocapacitive behavior. With increasing scan rates, the slight shift of the peaks manifests the small polarization and fast reaction kinetics during (de)intercalation of sodium ions. A related analysis is taken to investigate the reaction kinetics. The relationship between peak current (i) versus scan rate (ν) is based on Equation (1)^[10]

$$i = a\nu^b \quad (1)$$

The b -value of 0.5 indicates diffusion-controlled charge storage, whereas b -value of 1 means capacitive-dominated process. The

b -value is obtained by plotting the $\log(i)$ versus $\log(\nu)$ plots and fitting the linear slope (Figure 3d). The anodic and cathodic b -values are 0.925 and 0.835, respectively, which are much close to 1, indicating a capacitive-dominated charge storage process.

To quantify the capacitive contribution to the total capacity, a detailed calculation is conducted based on Equation (2)^[10]

$$i(V) = k_1 \nu + k_2 \nu^{1/2} \quad (2)$$

where $i(V)$ represents the measured current (i) at a fixed potential (V). $k_1 \nu$ and $k_2 \nu^{1/2}$ represent capacitive and diffusion-controlled current responses, respectively. The shaded region (Figure 3e) corresponds to the capacitive contribution area of pyridine- $V_2O_5 \cdot nH_2O$ at 1 mV s^{-1} , which occupies 78% of the whole capacity. However, the capacitive contribution of the pure $V_2O_5 \cdot nH_2O$ sample for sodium ion storage is 50.7% at 1 mV s^{-1} .^[15]

According to these results, the functions of pyridine for optimizing the electrochemical performance of $V_2O_5 \cdot nH_2O$ are summarized in Figure 3f. According to Acid–Base Proton theory, the H-bond is formed between PyH^+ and $V=O$ group from the layers. The strongly coupled interaction stabilizes the layered structure of $V_2O_5 \cdot nH_2O$ (Figure 1). This effect makes the layered spacing of pyridine- $V_2O_5 \cdot nH_2O$ remains unchanged during repeated Na^+ electrochemical insertion and extraction (Figure 3a,b), leading to greatly enhanced cycling stability (Figure 2b). In the meantime, the electronic conductivity is increased according to the higher dispersion of band structure in pyridine- $V_2O_5 \cdot nH_2O$ (Figure 1f–h and Figure S6, Supporting Information), which is beneficial for achieving fast charge–discharge rates.

The intercalation pseudocapacitive pyridine- $V_2O_5 \cdot nH_2O$ nanowires with remarkable high capacity and rate capability are very promising as an emerging cathode for assembling a novel SIC with high energy density accompanying with high power. Recently, the co-intercalation of $[Na\text{-diglyme}]^+$ into the graphite anode shows high coulombic efficiency and rate performance.^[39,40] Herein, graphic MCMB is chosen as an anode which shows the excellent electrochemical performance (Figure S10, Supporting Information). Figure 4a shows the schematic of pyridine- $V_2O_5 \cdot nH_2O$ /MCMB SIC: the Na^+ (de)intercalates into the pyridine- $V_2O_5 \cdot nH_2O$ and solvated $[Na\text{-diglyme}]^+$ (de) intercalates into graphite layers. The specific current, capacity, energy density, and power density of the full SIC are calculated based on the total mass of the cathode and anode. The charge and discharge curves at different specific currents ranging from 0.03 to 10 $A\ g^{-1}$ in a voltage window of 0.1–4 V are presented in Figure 4b, which reveals high reversibility even at high current

density. The corresponding capacities of pyridine- $V_2O_5 \cdot nH_2O$ /MCMB SIC are 53 $mAh\ g^{-1}$ at 0.03 $A\ g^{-1}$ and 38 $mAh\ g^{-1}$ at 2 $A\ g^{-1}$. More importantly, the capacity is still retained 27 $mAh\ g^{-1}$ at a current density up to 10 $A\ g^{-1}$, indicating an excellent rate capability (Figure S11, Supporting Information). The cycling performance and coulombic efficiency were subsequently characterized at 1 $A\ g^{-1}$ (Figure S12, Supporting Information). The capacity retention was 95% after 800 cycles with coulombic efficiency approaching 100%. The Ragone plots of pyridine- $V_2O_5 \cdot nH_2O$ /MCMB show the high energy density at extremely high power density (Figure 4c). It delivers a maximum specific energy density of $\approx 96\ Wh\ kg^{-1}$ at a power density of 59 $W\ kg^{-1}$. When the power density increases to 14 $kW\ kg^{-1}$, the energy density retains 37.5 $Wh\ kg^{-1}$. Compared with previously reported state-of-the-art sodium ion storage devices: graphene oxide films// $Na_2Ti_3O_7$,^[41] AC// $Nb_2O_5@C$,^[42] and AC// V_2O_5 ,^[38] our SIC device delivers the highest energy density at extremely high power density.

In summary, we demonstrate that the strategy of forming strongly coupled interaction interlayer of $V_2O_5 \cdot nH_2O$ is very effective to stabilize layered structure for rapid Na^+ storage. The intercalated pyridine stabilizes the layered structure and improves the electronic conductivity, further optimizing the cycling and rate performance. In the half-cell tests, the intercalation pseudocapacitive pyridine- $V_2O_5 \cdot nH_2O$ nanowires cathode shows a superior rate capability (112, 97, and 50 $mAh\ g^{-1}$ at 4, 8, and 30 $A\ g^{-1}$) and excellent cycling stability for 3000 cycles (a capacity retention of 67%). Putting a step forward to full device, the assembled pyridine- $V_2O_5 \cdot nH_2O$ /MCMB SIC shows a maximum energy density of $\approx 96\ Wh\ kg^{-1}$ at a power density of 59 $W\ kg^{-1}$, and a high power density of 14 $kW\ kg^{-1}$ at the energy

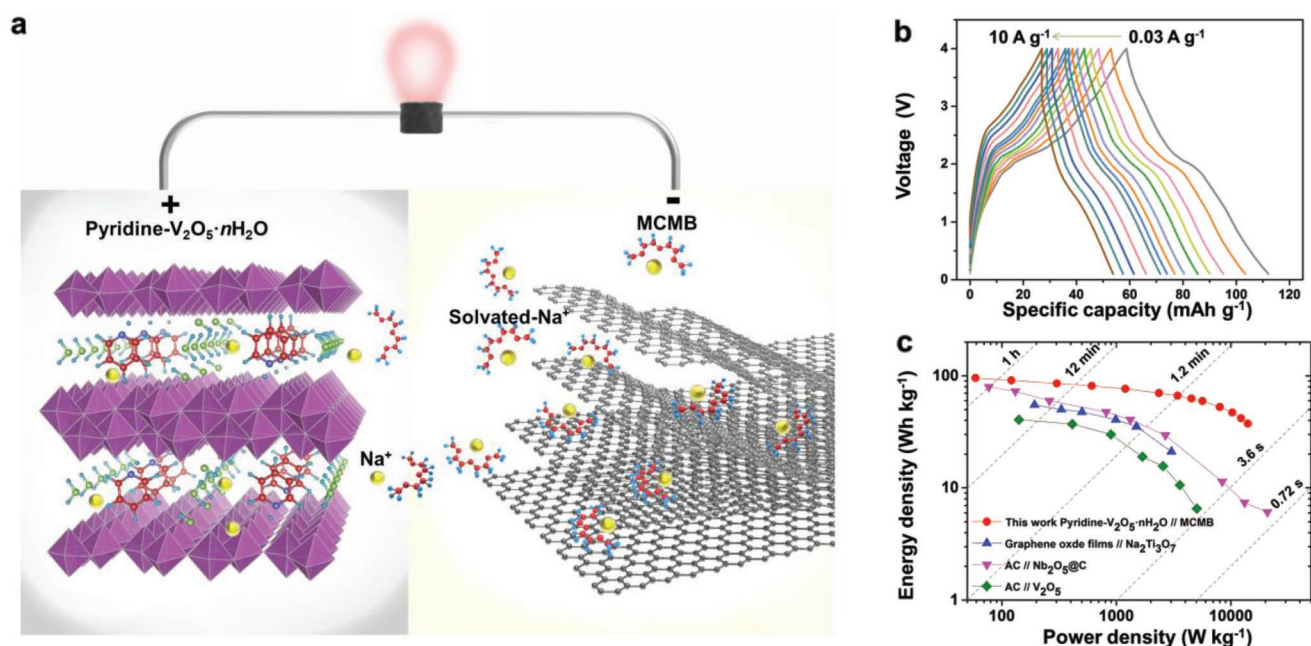


Figure 4. Electrochemical performance of pyridine- $V_2O_5 \cdot nH_2O$ /MCMB SIC. a) Schematic of pyridine- $V_2O_5 \cdot nH_2O$ /MCMB SIC: Na^+ (de)intercalates from the pyridine- $V_2O_5 \cdot nH_2O$ and the solvated $[Na\text{-diglyme}]^+$ (de) intercalates into graphite layers. b) Charge/discharge curves of pyridine- $V_2O_5 \cdot nH_2O$ /MCMB SIC at different current densities from 0.03 to 10 $A\ g^{-1}$, showing a high-rate capability. c) Ragone plots of the pyridine- $V_2O_5 \cdot nH_2O$ /MCMB and the reported state-of-the-art SICs: graphene oxide films// $Na_2Ti_3O_7$,^[41] AC// $Nb_2O_5@C$,^[42] and AC// V_2O_5 .^[38]

density of 37.5 Wh kg⁻¹. These results highlight the advantages of utilizing high-capacity pseudocapacitive cathode materials to set up the high energy SIC accompanying with high power. We believe that realizing the strongly coupled interaction between intercalated molecules and the layered materials (e.g., transition metal oxides/disulfides and MXenes) could lead to a wide range of opportunities for enhancing the overall performance of layered materials.

Supporting Information

Supporting Information is available from the Wiley Online Library or from the author.

Acknowledgements

This work was supported by the National Natural Science Fund for Distinguished Young Scholars (51425204), the National Key R&D Program of China (2016YFA0202601 and 2016YFA0202603), the National Natural Science Foundation of China (51602239, 51832004), the International Science & Technology Cooperation Program of China (2013DFA50840), and the Fundamental Research Funds for the Central Universities (WUT: 2017III009), the National Basic Research Program of China (2013CB934103).

Conflict of Interest

The authors declare no conflict of interest.

Keywords

pseudocapacitors, sodium ion capacitors, stabilized layers, strongly coupled interactions, V₂O₅·nH₂O

Received: January 22, 2019
Revised: March 21, 2019
Published online: April 24, 2019

- [1] J. Ding, W. Hu, E. Paek, D. Mitlin, *Chem. Rev.* **2018**, *118*, 6457.
[2] Y. Wang, Y. Song, Y. Xia, *Chem. Soc. Rev.* **2016**, *45*, 5925.
[3] V. Aravindan, J. Gnanaraj, Y. S. Lee, S. Madhavi, *Chem. Rev.* **2014**, *114*, 11619.
[4] K. Naoi, S. Ishimoto, J.-I. Miyamoto, W. Naoi, *Energy Environ. Sci.* **2012**, *5*, 9363.
[5] H. Wang, C. Zhu, D. Chao, Q. Yan, H. J. Fan, *Adv. Mater.* **2017**, *29*, 1702093.
[6] C. P. Grey, J. M. Tarascon, *Nat. Mater.* **2017**, *16*, 45.
[7] W. Luo, Y. Zhang, S. Xu, J. Dai, E. Hitz, Y. Li, C. Yang, C. Chen, B. Liu, L. Hu, *Nano Lett.* **2017**, *17*, 3792.
[8] L. Fan, X. Li, *Nano Energy* **2018**, *53*, 630.
[9] X. Wang, S. Kajiyama, H. Iinuma, E. Hosono, S. Oro, I. Moriguchi, M. Okubo, A. Yamada, *Nat. Commun.* **2015**, *6*, 6544.
[10] V. Augustyn, P. Simon, B. Dunn, *Energy Environ. Sci.* **2014**, *7*, 1597.
[11] V. Augustyn, J. Come, M. A. Lowe, J. W. Kim, P. L. Taberna, S. H. Tolbert, H. D. Abruña, P. Simon, B. Dunn, *Nat. Mater.* **2013**, *12*, 518.
[12] Q. Wang, J. Xu, W. Zhang, M. Mao, J. Ma, *J. Mater. Chem. A* **2018**, *6*, 8815.
[13] X. Liu, Y. Hao, J. Shu, H. M. K. Sari, L. Lin, H. Kou, J. Li, W. Liu, B. Yan, D. Li, J. Zhang, X. Li, *Nano Energy* **2019**, *57*, 414.
[14] M. Yu, Y. Zeng, Y. Han, X. Cheng, W. Zhao, C. Liang, Y. Tong, H. Tang, X. Lu, *Adv. Funct. Mater.* **2015**, *25*, 3534.
[15] Q. Wei, J. Liu, W. Feng, J. Sheng, X. Tian, L. He, Q. An, L. Mai, *J. Mater. Chem. A* **2015**, *3*, 8070.
[16] L. R. D. Jesus, J. L. Andrews, A. Parija, S. Banerjee, *ACS Energy Lett.* **2018**, *3*, 915.
[17] L. Mai, Y. Dong, L. Xu, C. Han, *Nano Lett.* **2010**, *10*, 4273.
[18] A. Pan, J. G. Zhang, Z. Nie, G. Cao, B. W. Arey, G. Li, S. Q. Liang, J. Liu, *J. Mater. Chem.* **2010**, *20*, 9193.
[19] R. Kiruthiga, C. Nithya, R. Karvembu, B. V. R. Reddy, *Electrochim. Acta* **2017**, *256*, 221.
[20] Q. Wei, Z. Jiang, S. Tan, Q. Li, L. Huang, M. Yan, L. Zhou, Q. An, L. Mai, *ACS Appl. Mater. Interfaces* **2015**, *7*, 18211.
[21] Y. Zhao, C. Han, J. Yang, J. Su, X. Xu, S. Li, L. Xu, R. Fang, H. Jiang, X. Zou, *Nano Lett.* **2015**, *15*, 2180.
[22] H. H. Kristoffersen, H. Metiu, *J. Phys. Chem. C* **2016**, *120*, 3986.
[23] H. P. Wong, B. C. Dave, F. Leroux, J. Harreld, B. Dunn, L. F. Nazar, *J. Mater. Chem.* **1998**, *8*, 1019.
[24] G. Zhang, T. Xiong, M. Yan, Y. Xu, W. Ren, X. Xu, Q. Wei, L. Mai, *Chem. Mater.* **2017**, *29*, 8057.
[25] J. M. Savariault, D. Lafargue, J. L. Parize, J. Galy, *J. Solid State Chem.* **1992**, *97*, 169.
[26] E. Ruizhitzky, B. Casal, *J. Chem. Soc., Faraday Trans. 1* **1986**, *82*, 1597.
[27] D. Cook, *Can. J. Chem.* **1961**, *39*, 2009.
[28] T. Yatabe, M. Nakano, G. Matsubayashi, *J. Mater. Chem.* **1998**, *8*, 699.
[29] Y. Song, T.-Y. Liu, B. Yao, T.-Y. Kou, D.-Y. Feng, X.-X. Liu, Y. Li, *Small* **2017**, *13*, 1700067.
[30] M. G. Kanatzidis, C. G. Wu, H. O. Marcy, D. C. DeGroot, C. R. Kannewurf, *Chem. Mater.* **1990**, *2*, 222.
[31] J. Harreld, H. P. Wong, B. C. Dave, B. Dunn, L. F. Nazar, *J. Non-Cryst. Solids* **1998**, *225*, 319.
[32] X. Xiang, K. Zhang, J. Chen, *Cheminform* **2015**, *46*, 5343.
[33] D. Su, G. Wang, *ACS Nano* **2013**, *7*, 11218.
[34] D. W. Su, S. X. Dou, G. X. Wang, *J. Mater. Chem. A* **2014**, *2*, 11185.
[35] H. Y. Li, C. H. Yang, C. M. Tseng, S. W. Lee, C. C. Yang, T. Y. Wu, J. K. Chang, *J. Power Sources* **2015**, *285*, 418.
[36] V. Raju, J. Rains, C. Gates, W. Luo, X. Wang, W. F. Stickle, G. D. Stucky, X. Ji, *Nano Lett.* **2014**, *14*, 4119.
[37] A. Moretti, F. Maroni, I. Osada, F. Nobili, S. Passerini, *ChemElectroChem* **2015**, *2*, 529.
[38] Z. Chen, V. Augustyn, X. Jia, Q. Xiao, B. Dunn, Y. Lu, *ACS Nano* **2012**, *6*, 4319.
[39] J. Zhang, D.-W. Wang, W. Lv, L. Qin, S. Niu, S. Zhang, T. Cao, F. Kang, Q.-H. Yang, *Adv. Energy Mater.* **2018**, *8*, 1801361.
[40] H. Kim, J. Hong, G. Yoon, H. Kim, K.-Y. Park, M.-S. Park, W.-S. Yoon, K. Kang, *Energy Environ. Sci.* **2015**, *8*, 2963.
[41] S. Dong, L. Shen, H. Li, G. Pang, H. Dou, X. Zhang, *Adv. Funct. Mater.* **2016**, *26*, 3703.
[42] E. Lim, C. Jo, M. S. Kim, M. H. Kim, J. Chun, H. Kim, J. Park, K. C. Roh, K. Kang, S. Yoon, *Adv. Funct. Mater.* **2016**, *26*, 3553.